Journal of Ocean Engineering and Science xxx (xxxx) xxx

Contents lists available at ScienceDirect

Journal of Ocean Engineering and Science

journal homepage: www.elsevier.com/locate/joes

A spectral coupled boundary element method for the simulation of nonlinear surface gravity waves

Kaiyuan Shi, Renchuan Zhu*, Dekang Xu

State Key Laboratory of Ocean Engineering, School of Naval Architecture, Ocean and Civil Engineering, Shanghai Jiao Tong University, Shanghai 200240, China

ARTICLE INFO

Article history:
Received 24 April 2023
Revised 25 June 2023
Accepted 12 July 2023
Available online xxx

Keywords:
Domain decomposition
Multi-domain method
Fully nonlinear
Wave–body interaction
Potential flow theory

ABSTRACT

The challenge of simulating the broad open sea with limited computational resources has long been of interest in ocean engineering research. In view of this issue, this paper proposes a fully nonlinear potential flow method named the spectral coupled boundary element method (SCBEM). By leveraging the approach of domain decomposition, SCBEM achieves significantly reduced computational cost and an order of magnitude increase in computational domain compared to the conventional boundary element method (BEM). The SCBEM encompasses the marine structure with only a tiny BEM domain and employs a high-order spectral layer to simulate the broad water outside the BEM domain. The performance of the SCBEM is evaluated through comparison with the wave damping approach and literature results for regular waves, modulated wave trains, focused waves, and diffraction of a vertical cylinder. The numerical results demonstrate the effectiveness and accuracy of the SCBEM in simulating a wide range of wavelengths and nonlinear wave interactions.

1. Introduction

Potential flow theory plays an important role in studies of water wave dynamics and wave–structure interactions. As hydrodynamic research has progressed and the focus on nonlinear wave behavior has increased, the fully nonlinear potential flow method has attracted increasing interest for its ability to account for nonlinear water surfaces and instantaneous wet body surfaces [1–5].

Despite significant advancements in computing power, the simulation of a broad range of nonlinear free surfaces remains a challenge. Numerical methods based on potential flow theory can be divided into two categories: spatial-based and boundary-based. The former, such as the finite element method (FEM), finite volume method (FVM), and harmonic polynomial cell (HPC) method [6], discretize the entire flow field into a highly detailed mesh to precisely capture the flow filed below the free surface. These methods often require discretizing a computational domain of around a dozen wavelengths into millions of grids, leading to computation times measured in days, even though only sparse matrices need to be solved.

Boundary-based methods, represented by the boundary element method (BEM), take advantage of the linearity of Laplace's equation to discretize only the boundary. In comparison to spatial-based methods, BEM requires fewer grids, however, the coefficient matrix solved by BEM is dense, resulting in a computational complexity of $O(N^2)$ for problems with N unknowns, even when utilizing iterative solvers like Generalized Minimal Residual method (GMRES). The development of algorithms such as the fast multipole algorithm [7] and Barnes–Hut algorithm [8] in the 1980s has significantly reduced the computational time of BEM simulations from $O(N^2)$ to $O(N)$ or $O(N\log N)$. Nevertheless, the size of the free surface that can be effectively simulated with the BEM remains limited. The current state-of-the-art in fully nonlinear potential flow simulations [2,5] involves a relatively modest number of grids, usually in the range of a few tens of thousands, and a computational domain limited to no more than 10 wavelengths. However, the simulation time for a single case still often takes tens of core-hours.

Due to limitations in computational efficiency, current numerical methods are usually limited to simulating small calculation domains. However, a considerable number of issues studied in the field of marine and ocean engineering occur in an open ocean setting, where platforms or ships encounter incident waves and generate scattering waves that propagate out to infinity. The phys-

* Corresponding author.
E-mail address: renchuan@sjtu.edu.cn (R. Zhu).

https://doi.org/10.1016/j.joes.2023.07.003

ical reality of unbounded seas and the finite computational domain form a contradictory pair. Therefore, it is necessary to utilize non-reflecting boundary conditions (NRBCs) when simulating an unbounded ocean [9–12]. The most widely used NRBC might be the wave damping technique, also known as numerical beach [13]. The computational domain is surrounded by a damping zone that reduces the energy of outgoing waves, preventing them from reflecting when they reach the truncation boundary. This approach is straightforward to implement and provides effective dissipation of high-frequency waves. However, its effectiveness is limited by the requirement that the width of the damping zone must be greater than the wavelength of the waves to be damped [10]. The utilization of dispersion relations as a means of converting a truncated boundary into a transparent one that permits wave transmission is also a widely researched area of NRBCs. The Sommerfeld–Orlanski condition, proposed by Orlanski [14], is a prominent example of this approach, permitting waves of a specific speed to pass through without hindrance. Since then, various radiation-type boundary conditions have been explored and designed [15–19], which allow for the transmission of waves through the truncation boundary for a specific range of velocities. Additionally, there have been efforts to combine the advantages of both damping layer and radiation conditions by integrating them, in order to effectively dissipate short waves while allowing long waves to pass through the boundary [10,20,21].

On the other hand, multi-domain methods, also known as domain decomposition methods, strives to simulate larger computational domains to better approximate the reality of unbounded ocean. One well-known approach (see [22–24]) involves treating the open sea outside the BEM computational domain as an outer domain, where the free-surface condition is linearized and described by the free-surface Green's function on the truncation BEM boundaries. The velocity matching condition at the truncation boundaries constitutes a special type of NRBC, allowing waves of any frequency to pass freely from the inner BEM domain. However, in nonlinear simulations, a large transition zone is required to gradually convert the nonlinear solution of the BEM domain to a linear form. Another promising strategy for modeling fully nonlinear problems uses Rankine sources for all decomposed subdomains [25]. By dividing the fluid domain into interconnected subdomains and matching the velocity at the shared boundaries, the equation solved by BEM is transformed from a dense matrix to a block-banded matrix, which can be solved by an optimized banded solver with reduced cost. To reduce the computational effort, De Haas and Zandbergen [26] solved the boundary value problem individually for each subdomain and iteratively matched the velocity/potential of the shared imaginary boundaries. Bai and Eatock Taylor [27,28], Geng et al. [29] further improved the iteration scheme of De Haas method.

In this paper, a novel domain decomposition method, the spectral coupled boundary element method (SCBEM), is presented as a solution to simulate the vast ocean. The SCBEM employs a compact BEM computational domain surrounding marine structures, and models the broader water surface outside the BEM domain with the high-order spectral (HOS) method. With regard to the internal BEM domain, the SCBEM may also be viewed as a specialized form of NRBC, allowing nonlinear waves to freely pass through the BEM boundary. Compared to conventional BEM, SCBEM entails significantly lower computational expenses and permits computational domains that are tens of times larger, which aligns better with the reality of unbounded ocean and concurrently enables investigation of far-field waves. While conventional BEM approaches require several hours to conduct fully nonlinear simulations of wave–structure interactions, SCBEM is capable of achieving the same results within a few minutes, demonstrating its potential for practical applications.

The paper is structured as follows: Section 2 provides an overview of the basic principles and numerical implementation of the SCBEM. In Section 3, we evaluate the performance of the SCBEM in handling nonlinear waves through a series of simulations. We compare the results of regular wave simulations with those obtained from the classical wave damping approach. Further, we examine the SCBEM's ability to model modulated wave trains, focused waves, and the diffraction around a vertical cylinder, and compare these results with those reported in the literature. Finally, the conclusions of this study are summarized in Section 4.

2. Mathematical model and numerical methods

2.1. Governing equations in the open sea

Consider a Cartesian coordinate system with the z-axis vertically upward and the origin located at the calm water surface. Assuming the fluid to be inviscid and incompressible and the flow to be irrotational, the flow field can be described by the velocity potential in the framework of potential flow theory:

$$\nabla^2\phi(\boldsymbol{x},z,t)=0 \tag{1}$$

$$(u,v,w)=\nabla\phi \tag{2}$$

where $\boldsymbol{x}\equiv(x,y)$ denotes the horizontal vector, (u,v,w) denotes the velocity field in the x, y, and z directions, respectively.

The free surface conditions are written under the Eulerian method as:

$$\left.\begin{aligned}\frac{\partial\zeta}{\partial t}&=\frac{\partial\phi}{\partial z}-\nabla_{\boldsymbol{x}}\phi\cdot\nabla_{\boldsymbol{x}}\zeta\\ \frac{\partial\phi}{\partial t}&=-g\zeta-\frac{(\nabla\phi)^2}{2}\end{aligned}\right\}\quad on\ S_f \tag{3}$$

where S_f denotes the free surface, $\zeta(\boldsymbol{x},t)$ is the free surface elevation, g is the gravitational acceleration, and $\nabla_{\boldsymbol{x}}\equiv(\partial/\partial x,\partial/\partial y)$ is the horizontal gradient.

As the instantaneous free surface varies with time, following Zakharov [30], we keep the horizontal coordinates of the control points unchanged and introduce the surface potential:

$$\phi^S(\boldsymbol{x},t)=\phi(\boldsymbol{x},\zeta(\boldsymbol{x},t),t) \tag{4}$$

Substituting Eq. (4) into Eq. (3), the chain rule allows the free surface conditions to be written as:

$$\left.\begin{aligned}\frac{\partial\zeta}{\partial t}&=\left(1+\left(\nabla_{\boldsymbol{x}}\zeta\right)^2\right)\frac{\partial\phi}{\partial z}-\nabla_{\boldsymbol{x}}\phi^S\cdot\nabla_{\boldsymbol{x}}\zeta\\ \frac{\partial\phi^S}{\partial t}&=\frac{1+\left(\nabla_{\boldsymbol{x}}\zeta\right)^2}{2}\left(\frac{\partial\phi}{\partial z}\right)^2-g\zeta-\frac{\left(\nabla_{\boldsymbol{x}}\phi^S\right)^2}{2}\end{aligned}\right\}\ on\ S_f \tag{5}$$

In addition to the free surface condition, the velocity potential ϕ must also satisfy the bottom boundary condition:

$$\frac{\partial\phi}{\partial z}=0\quad as\ z\to-\infty \tag{6}$$

And the boundary condition on solid body surface S_b:

$$\frac{\partial\phi}{\partial n}=(\boldsymbol{U}+\boldsymbol{\Omega}\times\boldsymbol{r})\cdot\boldsymbol{n}\quad on\ S_b \tag{7}$$

where $\boldsymbol{U}$, $\boldsymbol{\Omega}$ are the velocity and angular velocity of the body, respectively, and $\boldsymbol{r}$, $\boldsymbol{n}$ are the coordinates and unit normal of the surface points, respectively.

Once the initial values of free surface elevation ζ and velocity potential ϕ^S are known, along with the motion of the object, it is possible to solve the initial boundary value problem (IBVP) constructed by Eqs. (5)–(7) together with the initial conditions. The

key to solving this problem in the time domain lies in the evolution of the free surface condition given by Eq. (5). In order to calculate the temporal derivative, it is necessary to calculate $\nabla_{\boldsymbol{x}}\zeta$, $\nabla_{\boldsymbol{x}}\phi^S$, and $\partial\phi/\partial z$. While $\nabla_{\boldsymbol{x}}\zeta$ and $\nabla_{\boldsymbol{x}}\phi^S$ can be easily obtained using numerical methods such as FDM, solving for $\partial\phi/\partial z$ at each time step is critical in solving this IBVP.

At each time step, in order to obtain $\partial\phi/\partial z$ on the free surface, it is necessary to solve the following boundary value problem (BVP):

$$\begin{cases} \phi = \phi^S & on\ S_f \\ \dfrac{\partial\phi}{\partial n} = (\boldsymbol{U} + \boldsymbol{\Omega}\times\boldsymbol{r})\cdot\boldsymbol{n} & on\ S_b \\ \dfrac{\partial\phi}{\partial z} = 0 & as\ z\to-\infty \end{cases} \tag{8}$$

2.2. Spectral coupled boundary element method

2.2.1. Decomposition strategy

Eq. (8) defines the velocity potential ϕ through the imposition of the Dirichlet condition on the free surface, the Neumann condition on the solid surface, and the infinite depth condition. To solve for ϕ at each time step in fully nonlinear simulations, equations must be established at instantaneous boundaries. However, traditional BEM approaches become increasingly time-consuming as the computational domain expands. Even with fast algorithms such as FMM, ensuring convergence during iterative solving is difficult, necessitating careful design of pre-conditioners.

To overcome these challenges and efficiently solve Eq. (8), SCBEM leverages the linear nature of Laplace's equation by decomposing the original BVP into two parts. The velocity potentials ϕ^H and ϕ^R respectively satisfy the following boundary conditions:

$$\begin{cases} \phi^H = \mathcal{T}\phi^S & on\ S_{f*} \\ \dfrac{\partial\phi^H}{\partial z} = 0 & as\ z\to-\infty \end{cases} \tag{9}$$

$$\begin{cases} \phi^R = (1-\mathcal{T})\phi^S & on\ S_f \\ \dfrac{\partial\phi^R}{\partial n} = -\dfrac{\partial\phi^H}{\partial n} + (\boldsymbol{U} + \boldsymbol{\Omega}\times\boldsymbol{r})\cdot\boldsymbol{n} & on\ S_b \\ \dfrac{\partial\phi^R}{\partial z} = 0 & as\ z\to-\infty \end{cases} \tag{10}$$

Here $\mathcal{T}$ represents a transition function. The sum of ϕ^H and ϕ^R gives the velocity potential that satisfies the original boundary conditions in Eq. (8). Due to the presence of the body surface, holes may exist in the free surface where the ϕ^S and ζ become undefined. In Eq. (9), S_{f*} refers to the *virtual free surface* obtained after filling the holes in the original free surface S_f.

Although it may appear that the number of BVPs to be solved has increased by one, clever utilization of the transition function $\mathcal{T}$ can render Eqs. (9) and (10) more amenable to numerical solution. A rectangular coupling region is manually defined to encompass the area that cannot be simulated using the HOS method. Beyond this coupling region, the value of $\mathcal{T}$ remains constant at 1:

$$\mathcal{T} = \begin{cases} 1 - T_x T_y & \text{in the couping region} \\ 1 & \text{outside the coupling region} \end{cases} \tag{11}$$

In the coupling region, T_x and T_y take on the following form:

$$\begin{aligned} T_x &= \frac{1}{2}\left(\mathrm{erf}\left(\frac{4d_x}{l_x} - 2\right) + 1\right) \\ T_y &= \frac{1}{2}\left(\mathrm{erf}\left(\frac{4d_y}{l_y} - 2\right) + 1\right) \end{aligned} \tag{12}$$

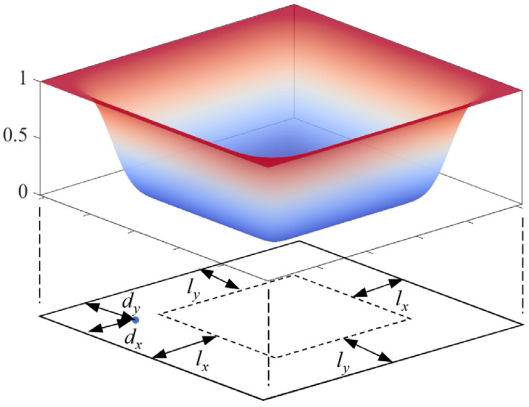

Fig. 1. Transition function $\mathcal{T}$ in the coupling region.

in which d_x, d_y are the minimum distances between a given position and the boundaries of the coupling zone along the x- and y-axes, respectively. The internal margin of the coupling region consists of a transition zone that with lengths of l_x and l_y along the x- and y-axes, respectively. As shown in Fig. 1, within this transition zone, the value of $\mathcal{T}$ gradually transitions from 1 to 0. As for the interior of the coupling region, the value of $\mathcal{T}$ remains fixed at 0.

If we place the object of interest within the coupling region, Fig. 2 demonstrates two BVPs that are divided using the transition function. Here, the color denotes the boundary value. By employing the transition function, the Dirichlet problem for ϕ^H becomes that of a near-field velocity potential with a zero boundary condition, as shown in the figure. On the other hand, ϕ^R needs to solve a Dirichlet-Neumann problem with a zero far-field velocity potential. For ϕ^H, the HOS method can be used to quickly obtain solutions, while the computational effort required to solve the BVP by BEM for ϕ^R will also be greatly reduced due to the presence of a zero far-field velocity potential.

2.2.2. Desingularized Rankine panel method

The present study implements a desingularized Rankine panel method (DRPM) to solve the BVP given by Eq. (10). Additional pertinent information can be found in [24,31]. As an indirect boundary element method, DRPM utilizes a superposition of Green's functions to express the velocity potential ϕ^R:

$$\phi^R(\boldsymbol{x}, z) = \sum\nolimits_i \sigma_i G_i(\boldsymbol{x}, z) \tag{13}$$

where G_i is the Green's function that satisfies Laplace's equation and deep-water bottom condition, and σ is the source strength.

Fig. 3 illustrates the discretization of the BEM domain. The free surface is discretized into a set of unstructured collocation points, with source points placed above these collocation points. In accordance with Eq. (5), the horizontal coordinates of the free-surface nodes remain constant while the vertical coordinates move with the free surface. Consequently, the vertical coordinates of both the collocation points and the source points situated above must be updated in each timestep, reflecting the wave elevation. The body surface is partitioned into triangular source panels, each having a collocation point situated at its center. This study uses a cutting-mesh method to obtain the instantaneous wet surface. Initially, a complete surface mesh is provided as input at the onset of the simulation. Subsequently, during each timestep, this complete mesh is intersected by the virtual free surface, yielding the wetted surface mesh beneath the waterline.

We denote the number of nodes on the free surface as N_f and the number of panels on the wetted body surface as N_b. The Green's function, G_i^{pt}, induced by the ith point source located at

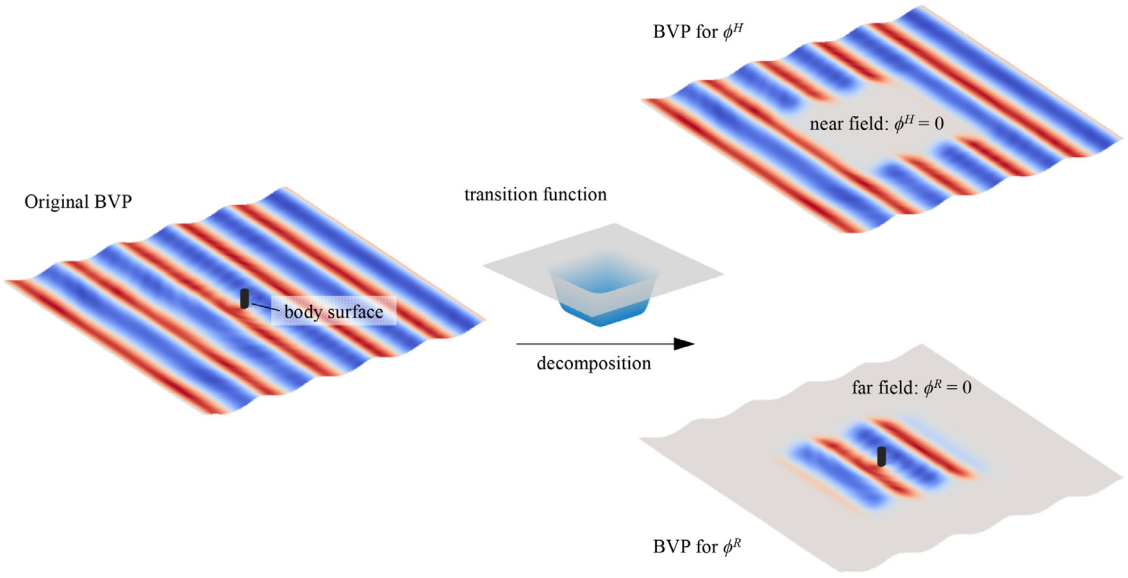

Fig. 2. Schematic diagram of the decomposition strategy. (color indicates the boundary value).

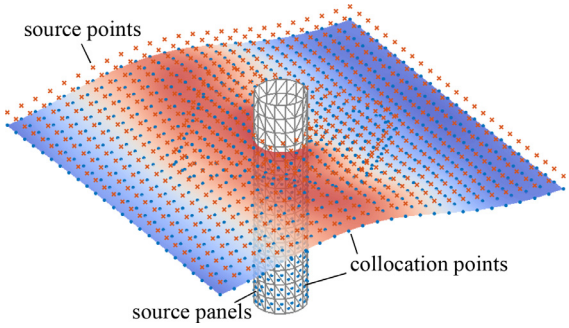

Fig. 3. Discretization of the BEM domain.

(ξ, η, ζ), is expressed as follows:

$$G_i^{pt}(x,y,z) = \frac{1}{\sqrt{(x-\xi)^2+(y-\eta)^2+(z-\zeta)^2}} \tag{14}$$

The Green's function G_i^{pan} for the ith panel source $(\xi, \eta, \zeta) \in S_i$ is given by:

$$G_i^{pan}(x,y,z) = \iint_{S_i} \frac{1}{\sqrt{(x-\xi)^2+(y-\eta)^2+(z-\zeta)^2}} dS \tag{15}$$

The source strength distribution, σ^{pt} and σ^{pan}, must satisfy the Dirichlet condition at the free surface collocation points:

$$\sum_{j=1}^{N_f} \sigma_j^{pt} G_j^{pt}(\boldsymbol{r}_i^{pt}) + \sum_{j=1}^{N_b} \sigma_j^{pan} G_j^{pan}(\boldsymbol{r}_i^{pt}) = \phi^R(\boldsymbol{r}_i^{pt}), \quad i = 1, 2, \ldots, N_f \tag{16}$$

Here the notation $\boldsymbol{r} \equiv (x, y, z)$, and $\boldsymbol{r}_i^{pt}$ represents the collocation point located beneath the ith source point.

At the collocation point $\boldsymbol{r}_i^{pan}$, which correspond to the center of the ith surface panel, σ^{pt} and σ^{pan} should fulfill the following Neumann conditions:

$$\sum_{j=1}^{N_f} \sigma_j^{pt} \frac{\partial}{\partial n_i} G_j^{pt}(\boldsymbol{r}_i^{pan}) + \sum_{j=1}^{N_b} \sigma_j^{pan} \frac{\partial}{\partial n_i} G_j^{pan}(\boldsymbol{r}_i^{pan}) = \frac{\partial}{\partial n_i} \phi^R(\boldsymbol{r}_i^{pan}), \quad i = 1, 2, \ldots, N_b \tag{17}$$

where n_i is the normal vector of the ith panel. As the collocation point $\boldsymbol{r}_j^{pan}$ coincides with the jth panel, the term $G_j^{pan}(\boldsymbol{r}_j^{pan})$ exhibits weak singularity. This singular integral can be accurately calculated using the analytical formula proposed by Hess and Smith[32]. Specifically, for the induced normal velocity, the following formula can be applied:

$$\frac{\partial}{\partial n_i} G_i^{pan}(\boldsymbol{r}_i^{pan}) = 2\pi \tag{18}$$

Once the source strengths are determined, the vertical velocity can be calculated as:

$$\frac{\partial \phi^R}{\partial z} = \sum_{j=1}^{N_f} \sigma_j^{pt} \frac{\partial G_j^{pt}}{\partial z} + \sum_{j=1}^{N_b} \sigma_j^{pan} \frac{\partial G_j^{pan}}{\partial z} \tag{19}$$

It can be observed that the Green's functions for Eqs. (14) and (15) exhibit a decay as the distance increases. When the field point and source are far apart, the induced velocity potential from the source can be neglected. Consequently, we confine the placement of sources within the coupling region and presume that ϕ^R satisfies the Dirichlet condition of $\phi^R(\boldsymbol{x}, \zeta) = 0$ outside the coupling region automatically. This assumption results in a notable reduction in the discretization required for solving Eq. (10) using BEM, thereby significantly enhancing computational efficiency. The effectiveness of this assumption will be analyzed in detail in subsequent sections.

2.2.3. High-order spectral method

This paper employs the HOS method to efficiently solve the Dirichlet problem of Eq. (9). The HOS method is a pseudo-spectral method that uses the Fast Fourier Transform (FFT) to efficiently solve the Dirichlet problem on nonlinear free surfaces. In this paper, only the formula for the HOS method is presented, with further details and derivations being available in the works of [33,34].

In cases involving the surface-piercing body, there exists a hole on the free surface. Moreover, the distribution of collocation points near the object is unstructured. To implement the HOS method, it is essential to first perform an interpolation of the free surface and then patch the hole caused by the presence of the object. This procedure eventually yields a virtual free surface represented by an equidistant grid as depicted in Fig. 4. The colors on the free surface indicate the Dirichlet condition of the velocity potential ϕ^H. It can

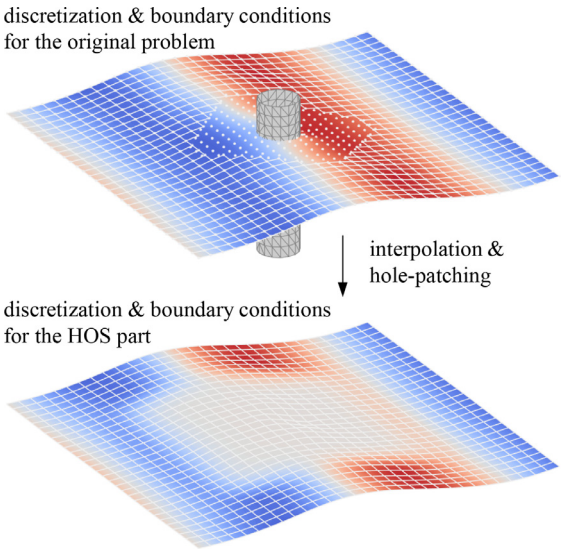

Fig. 4. The virtual free surface and the Dirichlet condition for ϕ^H.

be observed that although the free surface potential ϕ^S remains undefined at the hole. Due to the transition function being 0 in this area, the Dirichlet condition can be explicitly defined as 0.

Once the virtual free surface has been constructed and the boundary conditions in Eq. (9) have been established, one can effectively solve for the velocity potential ϕ^H with the HOS method. In the HOS method, ϕ^H is considered as a superposition of basis functions:

$$\phi^H(\boldsymbol{x}, z) = \mathrm{Re}\left(\sum_i A_i S_i(\boldsymbol{x}, z)\right) \tag{20}$$

where A is the amplitude of basis functions and S is the Fourier eigenfunction satisfying Laplace's equation and the deep-water bottom boundary condition:

$$S(\boldsymbol{x}, z) = \exp(|\boldsymbol{k}|z + i\boldsymbol{k}\cdot\boldsymbol{x}) \tag{21}$$

where $\boldsymbol{k} \equiv (k_x, k_y)$ is the wavenumber vector.

The ϕ^H at $z = \zeta$ can be expressed in various orders utilizing perturbation and Taylor expansions:

$$\phi^H(\boldsymbol{x}, z) = \sum_{i=1}^{\infty} \phi^{(i)}(\boldsymbol{x}, z) \ = \sum_{i=1}^{\infty}\left(\sum_{j=0}^{\infty} \frac{\zeta^j}{j!}\frac{\partial^j}{\partial z^j}\phi^{(i)}(\boldsymbol{x}, 0)\right) \tag{22}$$

Matching the orders of each term, the value of $\phi^{(i)}$ at $z = 0$ is given by the following equation:

$$\begin{aligned} &\phi^{(1)}(\boldsymbol{x}, 0) = \mathcal{T}\phi^S \\ &\phi^{(m)}(\boldsymbol{x}, 0) = -\sum_{k=1}^{m-1} \frac{\zeta^k}{k!}\frac{\partial^k}{\partial z^k}\left(\phi^{(m-k)}(\boldsymbol{x}, 0)\right), \ m > 1 \end{aligned} \tag{23}$$

and the surface vertical velocity $\partial\phi^H/\partial z$ is finally written as:

$$\frac{\partial}{\partial z}\phi^H(\boldsymbol{x}, \zeta) = \sum_{k=1}^{M}\left(\frac{\zeta^{k-1}}{(k-1)!}\frac{\partial^k}{\partial z^k}\sum_{m=1}^{M-k+1}\phi^{(m)}(\boldsymbol{x}, 0)\right) \tag{24}$$

where M is the truncation order of perturbation expansion, in this paper M is set to 3.

2.2.4. Further discussion

The BEM can solve Dirichlet–Neumann problems with complex geometries, but is quite time-consuming. The HOS method can quickly solve Dirichlet problems on nonlinear free surfaces, but only for uniform grids. The SCBEM aims to combine the advantages of both methods to simulate wave propagating in vast ocean with complex geometries at a small computational cost. It considers the total velocity potential as a superposition of two fundamental solutions:

$$\phi = \phi^R + \phi^H = \sum\nolimits_i \sigma_i G_i + \mathrm{Re}\left(\sum\nolimits_j A_j S_j\right) \tag{25}$$

The concept behind SCBEM is to determine a distribution of σ and A that fulfills the boundary conditions stated in Eq. (8). Here, σ is solved through the BEM approach, while A is obtained through the HOS approach. The Rankine source Green's function for BEM, G_i, exhibits singularity and locality. While the Fourier basis function for HOS, S_j, is global and does not contain any singularities. Recognizing the distinct descriptive capabilities of G_i and S_j, it is natural to propose a coupling scheme whereby G_i describes the near-field velocity potential while S_j characterizes the far-field. By utilizing this approach, BEM can be relieved of its responsibility in the far-field area, resulting in significant reductions in computational cost.

The derivation of SCBEM introduces only one non-rigorous assumption, namely that the distribution of source strength σ within the BEM domain satisfies the Dirichlet condition $\phi^R = 0$ outside the BEM domain. This paper refers to the approach of first solving the HOS part, followed by BEM to solve the residual within the coupling region as the Spectral–Green (S–G) approach. The S–G approach is not only justified by the decay properties of the Green's function $1/r$, but also because the induced velocity potential outside the BEM domain can be mutually cancelled due to the source strength distribution within the BEM domain. Numerical simulations presented later in this paper demonstrate that the S–G approach is sufficiently accurate in most cases.

Similarly, the SCBEM can also begin by constructing the BVP within the BEM domain and solving it before employing the HOS method to solve for the residuals. Such Green–Spectral (G–S) approach no longer assumes that the influence of the source strength distribution outside the BEM domain can be neglected, as in the S–G approach. Rather, it assumes that the impact of HOS on the body surface can be ignored, i.e., $\partial\phi^H/\partial n = 0$ in Eq. (10). To ensure mathematical rigor, it is also feasible to iteratively solve for both the BEM domain and the HOS layer to obtain σ and A that precisely satisfy the boundary conditions throughout the entire computational domain.

Although SCBEM is a fully nonlinear method, considering this issue from the perspective of linear time-domain Green's functions may enhance our understanding of the effective mechanism of SCBEM. The influence of the body surface can be regarded as a superposition of a series of impulse perturbations. Considering a impulse perturbation at $t = 0$, the impact of this perturbation on the flow field can be expressed as the following time-domain Green's function[35]:

$$\begin{aligned} G(P, Q, t) = &\left(\frac{1}{r} - \frac{1}{r_1}\right)\delta(t) \\ &+ 2\int_0^{\infty} \sqrt{gk}e^{k(z+\zeta)}J_0(kR)\sin\left(\sqrt{gk}t\right)dk \end{aligned} \tag{26}$$

where $P \equiv (x, y, z)$ and $Q \equiv (\xi, \eta, \zeta)$ denote the field point and source point, respectively. r is the distance between PQ, and r_1 is the distance between the field point and the mirror source point about the free surface. Eq. (26) consists of a impulsive term which indicate the immediate influence of the pulse excitation, and a memory term accounts for the memory effect of the free surface.

The impulsive term of the time-domain Green's function demonstrate singularity solely at the source point Q. In SCBEM, the panels placed on the body surface facilitate the modeling of the $1/r$ term, while the $1/r_1$ term is described by desingularized source points and HOS basis functions. The impulsive terms induce zero velocity potential on the free surface, while the induced

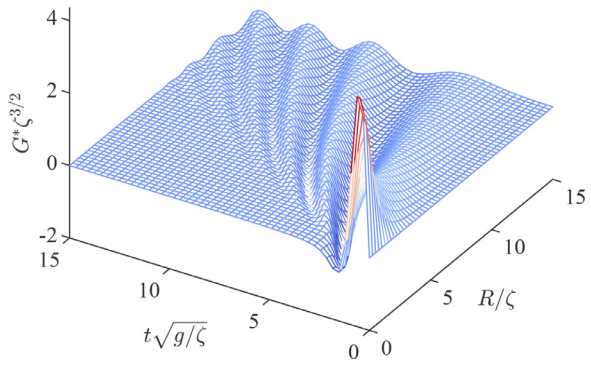

Fig. 5. Temporal and spatial variation of the memory term in the time-domain Green's function.

vertical velocity is ζ/r^3, which exhibits rapid decay with distance cubed. Therefore, when the free surface outside the BEM domain is remote from the body surface, the influence of impulsive term can even be numerically neglected.

Fig. 5 illustrates the influence of the memory term on the free surface, where R denotes the horizontal distance between the source point and the field point. At $t = 0$, it can be observed that the impulse-induced memory term has no effect on the free surface. During the ensuing brief period, only the nearby free surface experiences disturbance. As analyzed earlier regarding the impulsive terms, we can deduce that the effect of a disturbance can be categorized into two parts: the impulsive part, which only has a significant impact on the near field and a negligible effect on the far-field; and the memory part, which manifests as waves that gradually propagates outward with time.

From this perspective, despite the fact that the fluid is incompressible, owing to the presence of the free surface, the entire system does not exhibit significant long-range effects. Any disturbance will transform into surface gravity waves, which can be considered as satisfying the convective equation and progressively propagating according to the dispersion relationship. Therefore, regardless of the existence of solid surfaces, as long as SCBEM allows waves to flow into and out of the BEM domain undisturbed, hydrodynamic phenomenon can be correctly simulated.

2.3. Wave generation and absorption

Although SCBEM implements an HOS layer to simulate wide water bodies distant from the body surface and models a computation domain significantly larger than conventional BEM, the computation domain is ultimately limited. Without appropriate handling, scattered waves may approach the boundaries of the computation domain after long-time simulation and adversely affect the simulation. Two approaches, namely the periodic mode and the wave tank mode, are employed in this study to perform wave generation and absorption.

The periodic mode employs a relaxation method. We denote the velocity potential and wave elevation simulated by SCBEM as ϕ_t^S and ζ_t, respectively, and consider the nonlinear incident wave ϕ_i^S and ζ_i in the absence of the solid surface. After each time step calculation, the scattered waves generated by the presence of the object are absorbed using a relaxation function:

$$\begin{aligned}\zeta_t &= \zeta_i + R(x,y)(\zeta_t - \zeta_i)\\ \phi_t^S &= \phi_i^S + R(x,y)(\phi_t^S - \phi_i^S)\end{aligned} \tag{27}$$

Here $R(x,y)$ is a ramp function, written as:

$$R(x,y) = \exp\left(-\left(\frac{2x}{L_x}\right)^{12} - \left(\frac{2y}{L_y}\right)^{12}\right) \tag{28}$$

where L_x, L_y is the length of the SCBEM computational domain, and the coordinate origin is located at the center of the computational domain. In Eq. (27), the ϕ_i^S and ζ_i of the nonlinear incident wave field is obtained from a pure HOS simulation without any structures, which has the same computational domain and grid space as that of SCBEM. Specifically, at the initial time, the entire computational domain is given with the wave elevation and velocity potential. Under periodic boundary conditions, waves propagate periodically throughout the domain in the HOS simulation, thereby furnishing insights into incident waves in the absence of marine structures.

The wave tank mode behaves more like a physical wave tank, with a wave-making zone upstream and a damping zone downstream [36]. Both wave-making and wave-absorbing zones are well outside the coupling region. The incident waves are artificially coupled in the wave-making zone, consistent with Eq. (27). However, in the wave tank mode, $R(x,y)$ is only non-zero in the upstream wave-making zone, written as:

$$R(x,y) = 1 - \exp\left(-10\left(\frac{8x}{L_x} + 3\right)^{10}\right) \tag{29}$$

The section at the downstream end of the tank, measuring $L_x/4$ in length, is designated as the wave-absorbing zone. Within this zone, a dissipation term is added to Eq. (5) to absorb the waves:

$$\frac{\partial \phi^S}{\partial t} = -\nu\phi^S + \frac{1+\left(\nabla_{\boldsymbol{x}}\zeta\right)^2}{2}\left(\frac{\partial \phi}{\partial z}\right)^2 - g\zeta - \frac{\left(\nabla_{\boldsymbol{x}}\phi^S\right)^2}{2} \tag{30}$$

where ν is the Rayleigh viscosity, representing the strength of the dissipation. The value of ν transitions gradually from 0 to $0.36\sqrt{g/L_x}$ within the wave-absorbing zone. It is commonly accepted that the efficacy of wave absorption is relatively insensitive by ν, with the length of the absorption zone being the primary determinant of wave absorption effectiveness [37]. Traditional methods typically position the absorption zone within the BEM domain. However, such strategy requires a delicate balance between computational complexity and absorption effectiveness. An absorption zone that is too small may lead to insufficient wave absorption, while an overly large absorption zone can increase the computational burden. In contrast, the SCBEM situates the absorption zone outside the BEM domain. This arrangement minimizes the discretization within the BEM domain and ensures an adequate length for wave absorption, thereby guaranteeing the effectiveness of wave absorption.

2.4. Numerical implementation

In this study, the fourth-order Runge–Kutta method is employed for the numerical integration of the system of equations represented by Eq. (5). The flowchart in Fig. 6 illustrates the computation process for SCBEM. The algebraic system of the BEM domain is solved using a GMRES solver. The gradual transition of the boundary conditions to zero makes the iterative convergence straightforward, and hence, no preconditioner is used in the GMRES solution process.

To eliminate the *saw-tooth instability* that may occur during nonlinear time-domain simulations, a seven-point filter is applied to the HOS layer at each timestep and radial basis function interpolation with a smooth factor is applied to the collocation points to dissipate the high-frequency energy.

The numerical model delineated previously is implemented by using a mix of Fortran and C languages. To leverage the capabilities of the GPU, OpenCL kernels are employed to compute the influence coefficients of the Rankine sources and speed up the matrix operations for the HOS calculation. Simulations are performed in single precision using an AMD 3700X processor and an Nvidia RTX

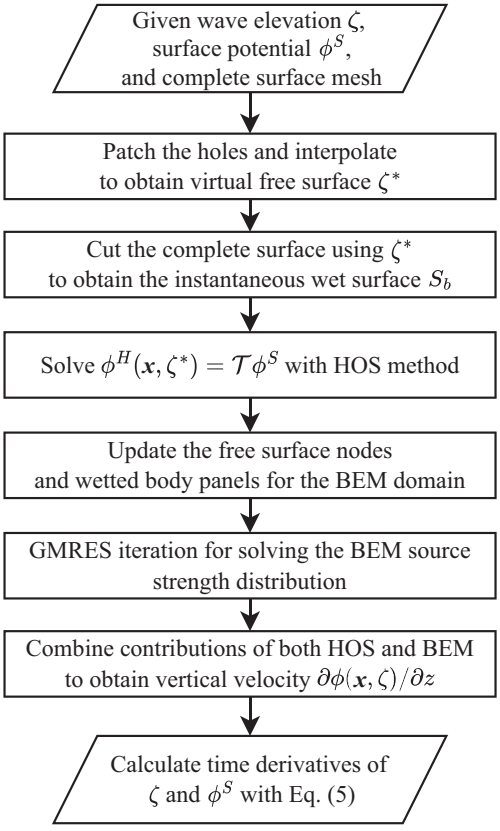

Fig. 6. Flowchart for computing temporal derivatives of the flow field using SCBEM.

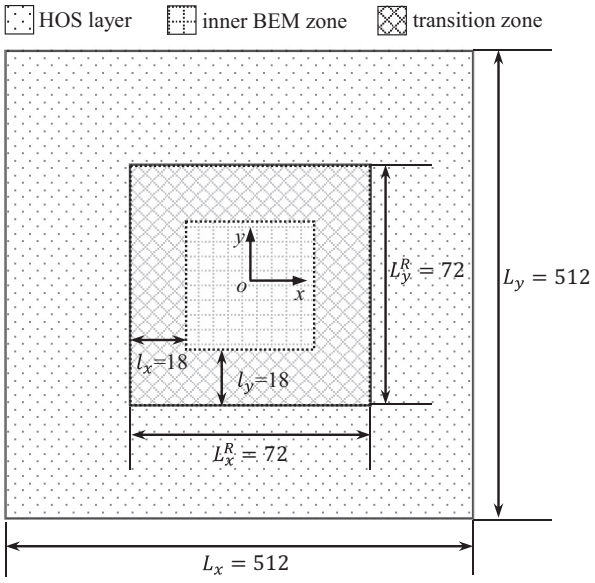

Fig. 7. Dimensional parameters of the domain.

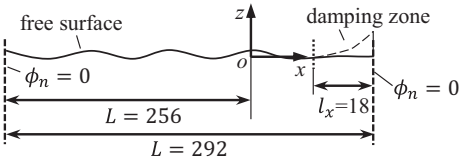

Fig. 8. Dimensional parameters of the wave-damping simulations.

2060 graphics card. For a case consisting of approximately 250,000 nodes and 6000 Rankine sources, the computational time for each time step is approximately 0.3 s, with the elapsed time ratio between the BEM domain and the HOS layer being roughly 40:1.

3. Numerical validation and discussion

3.1. Overview

This section presents a comprehensive validation of the SCBEM. As analyzed in Section 2, the effectiveness of the SCBEM is dependent on whether waves can propagate into and out of the BEM domain without interference. Thus, the first step towards validation entails conducting numerical simulations of regular waves. By examining the errors in simulating regular waves with different wavelengths as they propagate and enter/exit the BEM domain, a comprehensive understanding of the SCBEM's wave transmission capabilities can be gained. Subsequently, this section validates SCBEM's capability to simulate strong nonlinear phenomena such as modulated wave trains and focused waves. Finally, this section replicates the wave run-up of a cylinder and compares it to benchmark experiments.

The computational domain applied in this section is shown in Fig. 7, with the origin of the coordinate system located at the center. Denoting the grid spacing as 1 unit length, the BEM domain, positioned at the center, has a dimension of 72×72 and is enveloped by a larger HOS layer with a size of 512×512. The width of the transition zone is 18.

3.2. Regular waves

This subsection conducts a series of regular wave tests. The purpose of these tests is twofold: (1) To assess the efficacy of the SCBEM in transmitting waves of varying wavelengths through a convergence analysis of the parameter λ/l_x, which represents the ratio of the wavelength to the width of the transition zone. (2) To determine an appropriate range of wavelengths for conducting subsequent simulations of nonlinear waves.

The SCBEM can also be considered as a special type of NRBC added to the BEM domain, which effectively prevents unreasonable wave reflections at the boundary of the BEM domain. Therefore, this section also presents a comparison of the effectiveness between the SCBEM and the wave damping method. Numerical simulations with wave damping method are performed using the traditional BEM. As shown in Fig. 8, the width of the damping zone is consistent with that of the transition zone in the SCBEM, at 18 units. The wave-damping simulations adopt Eq. (30) to dissipate the waves in the damping zone. Following Boo [38], ν is written as:

$$\nu = \nu_0 \left(\frac{x - x_b}{l_x} \right)^2 \tag{31}$$

where $l_x = 18$ is the length of the damping zone, $x_b = 18$ is the start point of the damping zone. The constant ν_0 is determined through artificial means to achieve optimal damping performance.

Deep-water fifth-order Stokes waves are set as the incident waves [39]. For convenience, the grid spacing is set to 1m in this subsection. The chosen wave steepness for the numerical simulations is $kA = 0.01$, and the timestep selected is 1/36 of the wave period.

Fig. 9 compares the wave profiles at the midline of computational domain, which are simulated by SCBEM and damping method, respectively. Both methods use the wave tank mode, as

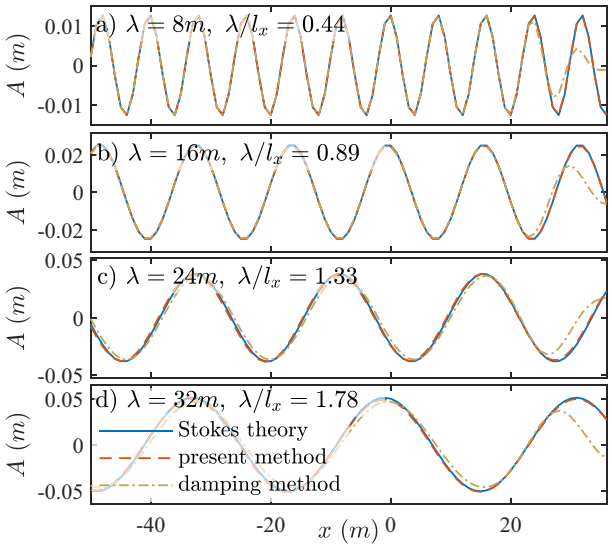

Fig. 9. Wave profiles of different wavelengths simulated with the SCBEM and damping approaches.

described in Section 2.3, to generate incident waves. And the wave-making zones are positioned in the same manner for both methods. In the SCBEM simulation, waves are created in the HOS layer outside the BEM domain, pass through the first transition zone ($x \in [-36, -18]$) into the inner BEM domain, propagate 36m within the BEM domain, then exit through the second transition zone ($x \in [18, 36]$) into the outside HOS layer. In the wave-damping simulation, the waves kept propagating and reached the damping zone located at $x \in [18, 36]$. The region $x \in [18, 36]$ in both methods served to prevent wave reflection at the truncated boundary ($x = 36$) of the BEM domain. Both methods produce good reflection-free results for $\lambda/l_x < 1$, but the damping method fails to fully dissipate the waves for $\lambda/l_x > 1$, as shown in Fig. 9(c) and (d). The reflected waves disturbed the original incident waves, causing deviation from the theoretical amplitude and phase, as also reported by Romate [10]. Unlike the conventional damping method, the SCBEM is capable of producing more accurate wave simulations, even when the wavelength exceeds the width of the transition zone. This suggests that the SCBEM is applicable to a much wider range of wavelengths than the damping method.

Fig. 10 illustrates the time history of the wave elevation at the center of the BEM domain. Both the periodic and wave tank modes exhibit good accuracy for a wide range of wavelengths, from a short wave with a wavelength of 8 grid units to a long wave with a wavelength of 64 grid units, and the waves generated by both methods are consistent with the theoretical solution. This highlights the accuracy and practicality of the SCBEM.

Fig. 11 displays the wave profiles in the wave tank mode at different times. The wave profiles progress from the start of the simulation to the steady state and are shown from top to bottom. When $\lambda = 8, 16, 32$, the BEM domain is effectively integrated with the HOS layer. However, for $\lambda = 64$, disturbances emerge in the water surface, particularly at the truncated BEM boundaries.

The relative error of a single probe is obtained by applying an FFT to its steady-state time history of wave elevation and comparing the frequency components with the theoretical solution:

$$Err = \frac{\|\mathcal{F}(\zeta(t)) - \mathcal{F}(\tilde{\zeta}(t))\|_2}{\|\mathcal{F}(\tilde{\zeta}(t))\|_2} \tag{32}$$

where $\mathcal{F}$ denotes the FFT operator, $\zeta(t)$ is the wave elevation recorded at the probe, and $\tilde{\zeta}(t)$ is the theoretical wave elevation.

We consider the fluid domain to have reached the steady state after 50 periods. The next 20 periods are used for the error analysis. The errors are calculated at each of the 72×72 collocation points and averaged to obtain the overall relative error for the whole BEM domain, as shown in Fig. 12. The results show that the SCBEM produces accurate results (errors less than 5%) for most cases, even when the wavelength is several times greater than the transition zone width. However, the error increases with the increasing wavelength. This is due to the steepness of the transition

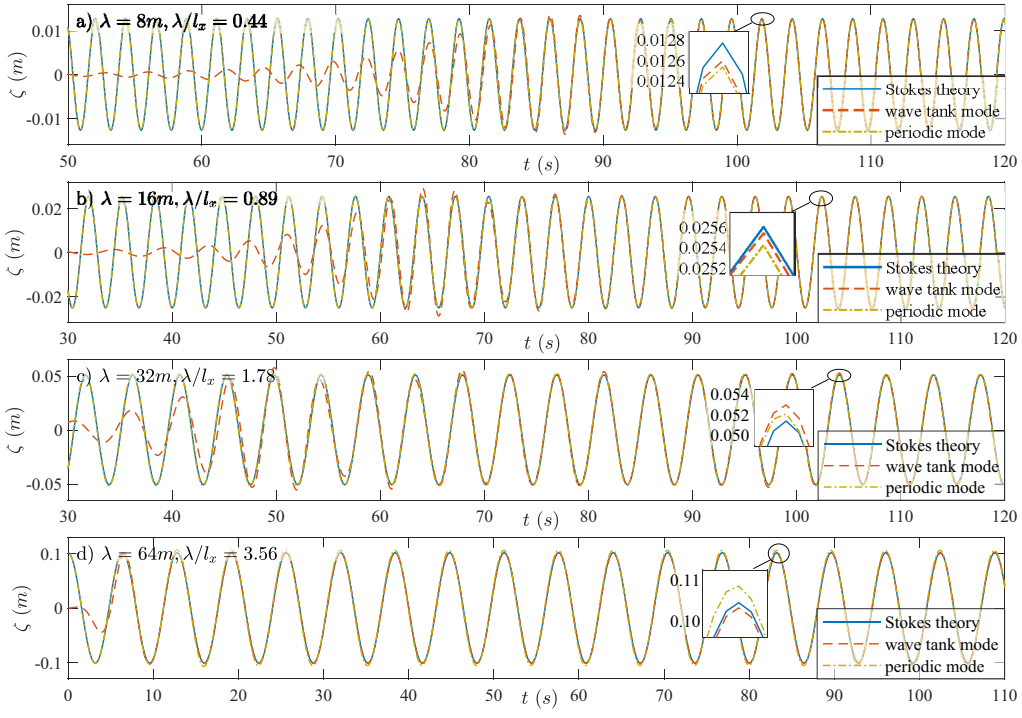

Fig. 10. Wave elevation at the center of the domain.

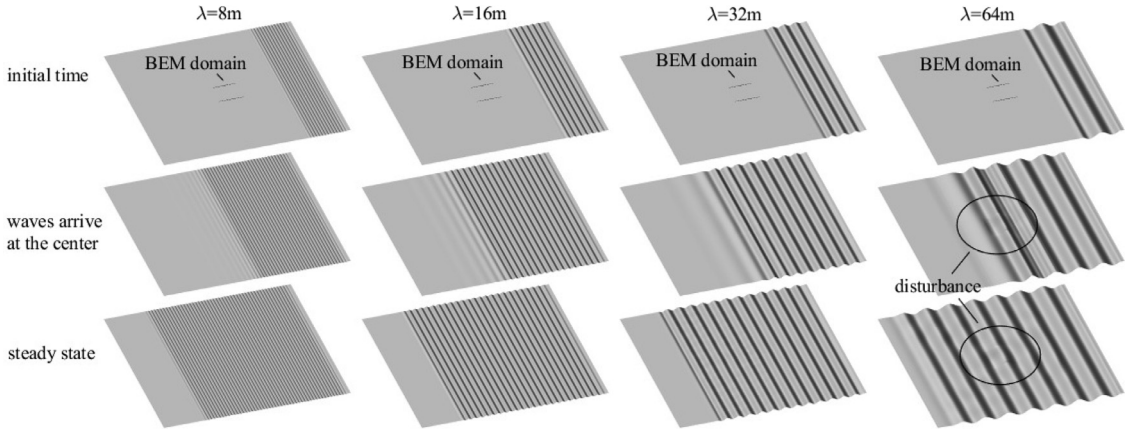

Fig. 11. Wave profiles of different wavelengths (wave tank mode).

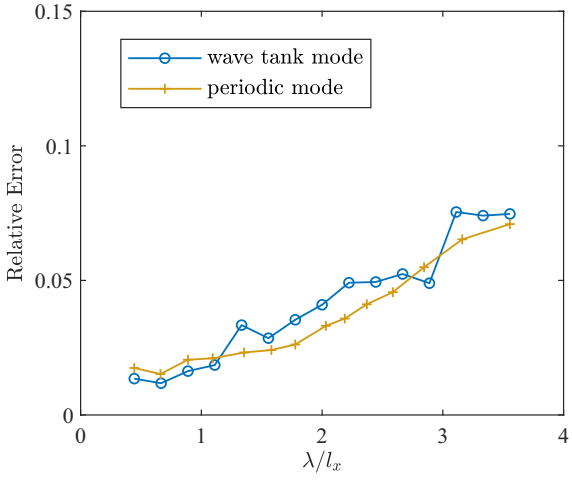

Fig. 12. Relative error of waves with different wavelengths.

function with respect to large wavelength waves, which leads to a velocity potential that does not satisfy the Dirichlet condition $\phi^R(\boldsymbol{x}, \zeta) = 0$ outside the BEM domain. To maintain accuracy, the wave lengths in subsequent simulations are kept within $\lambda/l_x < 2$.

3.3. Modulated wave trains

As pointed out by Zakharov [30], the third-order nonlinearity may lead to instabilities and energy transfer between wave components. This modulational instability (also called the Benjamin–Feir instability) plays an important role in realistic sea waves and makes a significant contribution to wave breaking and spectrum evolution [40,41]. To ensure that the SCBEM can properly model the nonlinear interactions between waves, modulated wave trains are simulated in the periodic mode. The initial conditions are consistent with the study by Iafrati et al. [42] on wave breaking, where ζ and ϕ^S are written as:

$$\begin{aligned}\zeta &= A_0\cos(k_0x) + A_1\cos(k_-x) + A_1\cos(k_+x)\\ \phi^S &= A_0\sqrt{g/k_0}\exp(k_0\zeta)\sin(k_0x)\\ &\quad + A_1\sqrt{g/k_-}\exp(k_-\zeta)\sin(k_-x)\\ &\quad + A_1\sqrt{g/k_+}\exp(k_+\zeta)\sin(k_+x)\end{aligned} \tag{33}$$

where $A_1 = 0.1A_0$, k_0 is the wavenumber of the major component, and the wavenumber of the sidebands is $k_\pm = k_0 \pm \Delta k$, with $\Delta k = k_0/5$.

The wavelength λ_0 of the major component is 512/20. And the initial wave steepness $\varepsilon_0 = k_0A_0$ is used to indicate the strength of the nonlinearity. Iafrati et al. [42] conducted simulations of wave evolution from the beginning until just before breaking using BEM for ε_0 values ranging from 0.12 to 0.18, and then imported the potential results into a Navier–Stokes solver for further study of wave breaking. The time history of wave components calculated using the SCBEM is compared to Iafrati's BEM results in Fig. 13. As a result of modulational instability, the waves in the fluid domain are not simply superimposed in a linear manner, with significant nonlinear energy transfer occurring between the main component and the sidebands. The time histories obtained from the two methods show good agreement, demonstrating that the SCBEM not only allows for the BEM domain to receive and transmit regular waves, but also simulates the nonlinear interactions between waves.

Fig. 14 compares the wave profiles before wave breaking given in Iafrati et al. [42] with the wave profiles in the midline of the SCBEM computational domain. The wave profiles obtained by the two approaches are in good agreement. Although the length of the BEM domain in the simulations ($2.8\lambda_0$) is shorter than the length of a wave packet ($5\lambda_0$), the SCBEM uses a transition zone ($0.7\lambda_0$) to embed the truncated BEM computational domain within a larger background domain, enabling the modulational instability of the wave trains to be accurately simulated. The results show that with the SCBEM, it is possible to simulate nonlinear phenomena occurring in a much larger sea area with a small BEM computational domain.

3.4. Focused waves

To further validate the ability of the SCBEM in simulating the interaction of a large number of wave components, this subsection reproduces the unidirectional focused wave experiments of Johannessen and Swan [43]. The experiments were conducted in a wave basin with a length of 11 m and a depth of 1.2 m. The wavemaker created wave components with equal amplitudes and frequency spacings, which formed a focused wave 5.5 m from the wavemaker according to linear theory.

This subsection proceeds with the computational domain shown in Fig. 7, but the grid spacing is set to 0.082 m. The simulations are performed in wave tank mode; according to linear theory, the waves will be focused at the center of the wave tank, where $x = 0$. For consistency with the experiment, the ramp function of the wave tank mode is shifted so that the wave-making section ends at $x = -5.5$ m.

Fig. 15 presents the time histories of the wave elevation at the position of maximum crest elevation. The numerical results

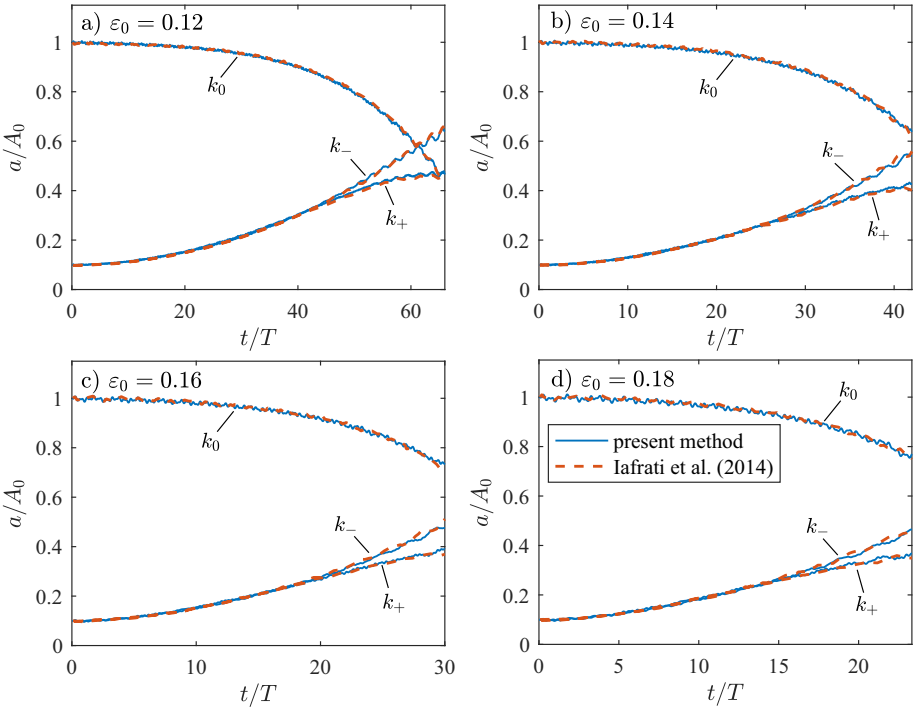

Fig. 13. Time history of wave components.

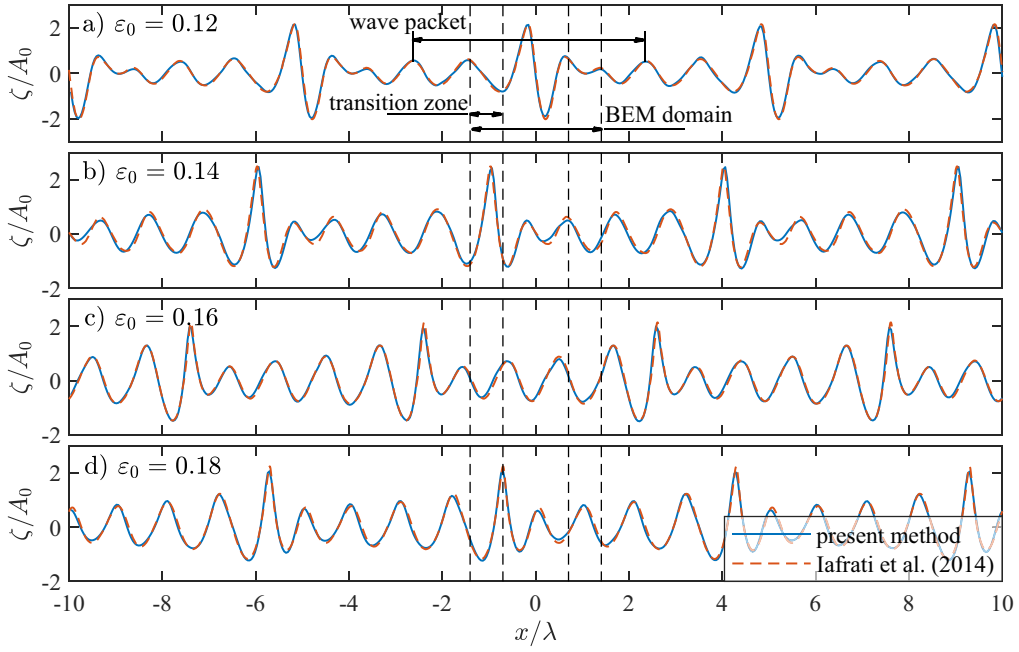

Fig. 14. Wave profiles in the midline of the SCBEM computational domain.

are compared with case D in the experiments of Johannessen and Swan [43], which contain 28 components with frequencies ranging from 53/64 Hz to 80/64 Hz at intervals of 1/64 Hz. The parameter A denotes the sum of the wave component amplitudes, which is also the maximum crest elevation in linear theory. As can be seen in Fig. 15, strong nonlinear effects occur during focusing, resulting in wave crests much higher than the linear prediction. The numerical results are in good agreement with the experiments, indicating that the SCBEM is capable of simulating nonlinear interactions between numerous wave components.

3.5. Diffraction around a cylinder

To validate the performance of the proposed method in simulating nonlinear wave–body interactions, wave diffraction around a truncated vertical cylinder is studied. This section numerically replicate the benchmark experiments organized by the Ocean Engineering Committee of the 27th International Towing Tank Conference [44].

The benchmark experiments were performed at MOERI using a truncated cylinder with a radius of 8 m and a draft of 24 m.

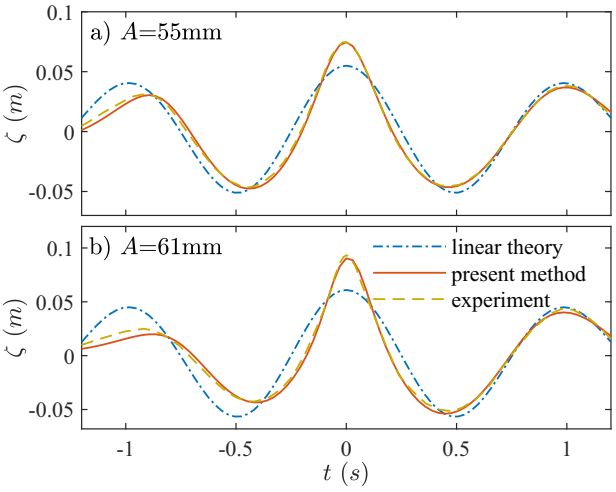

Fig. 15. Time histories of wave elevation at the position of maximum crest elevation.

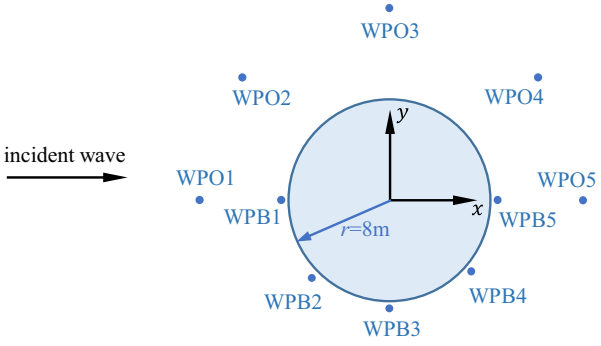

Fig. 16. Layout of wave probes.

To measure the time history of the wave elevation, several wave probes were placed around the cylinder, as shown in Fig. 16. Probes WPB1–WPB5 were placed uniformly at 45-degree intervals and positioned 8.206 m from the cylinder's center. Probes WPO1–WPO5 were located farther from the cylinder and placed at a distance of 16m from the center. This section simulates a regular wave with a period of $T = 9$ s and a wave steepness of $H/L = 1/16$, where the incident wave for the SCBEM simulation is generated using the wave tank mode.

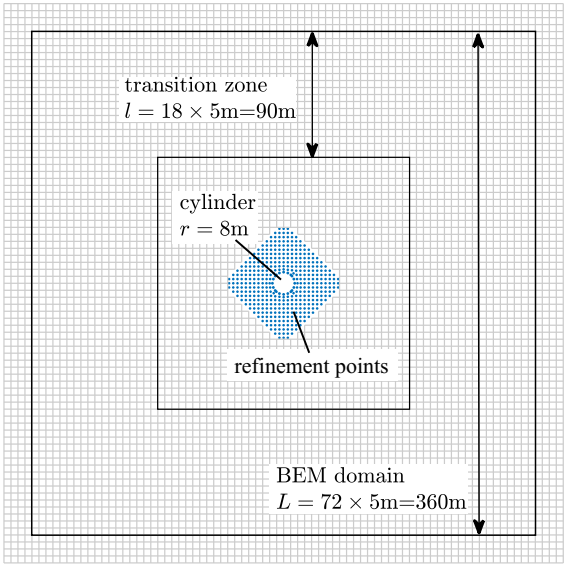

Fig. 17. Discretization for the BEM domain.

In numerical simulation, a cylinder is introduced at the center of the BEM domain, and the collocation points around it are refined, as illustrated in Fig. 17. The simulation adopts a time step of $\Delta t = T/45 = 0.2$ s, and it takes 18.1 s of wall time to simulate per wave period after reaching a steady state.

Fig. 18 presents a panoramic view of the entire computational domain and the wave pattern near the cylinder simulated by the proposed SCBEM. It can be seen that the SCBEM simulates a considerably large free surface area, with a length and width of over 300 times the radius of the cylinder, which is closer to the physical reality of an unbounded ocean. In Fig. 18(b), scattered wave patterns can be observed radiating outwards from the cylinder. These scattered waves successfully pass through the transition zone and enter the HOS layer outside the BEM domain, verifying the feasibility of the SCBEM.

Fig. 19 shows the time history of wave elevation at wave probes after reaching periodic steady state in the simulation. The SCBEM results are compared with experimental data and the numerical results using OpenFOAM by Sun et al. [45]. Both the proposed numerical method and the OpenFOAM simulation provide good predictions that agree well with the experiment. This indicates that the SCBEM effectively allows scatter waves to propagate freely

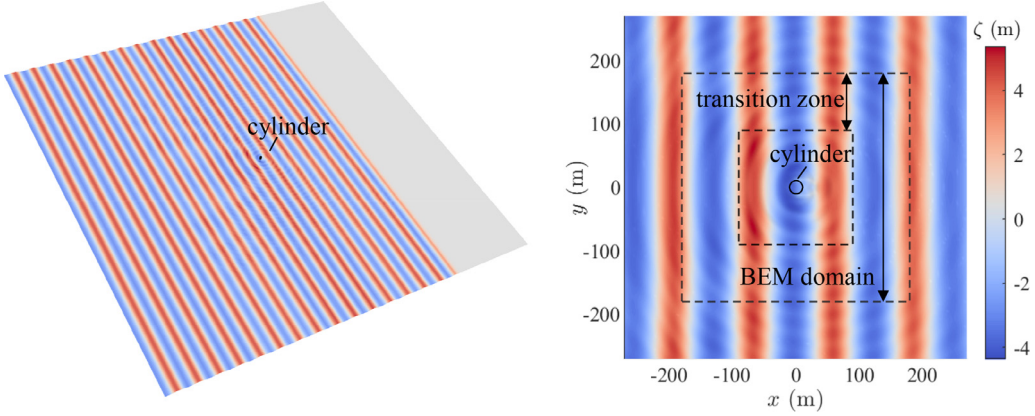

(a) wave pattern of the computional domain (b) wave pattern surround the cylinder

Fig. 18. Wave pattern of the SCBEM simulation.

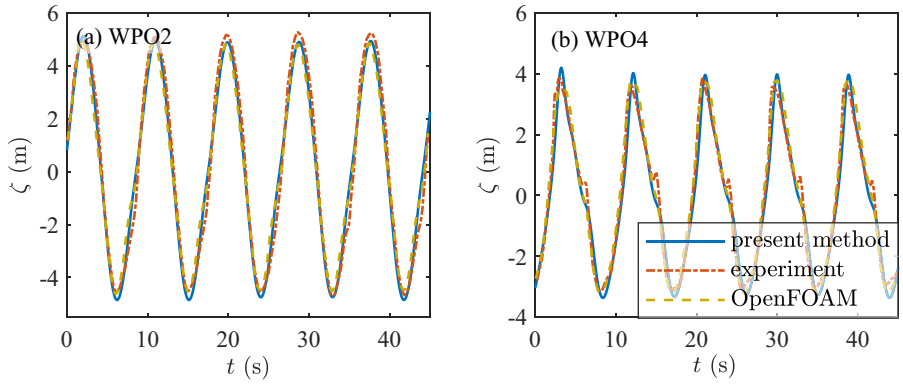

Fig. 19. Time history of surface elevation at wave probes: (a) WPO2 (b) WPO4 .

outside the BEM domain without causing any undesired reflected waves that could disturb the flow field.

4. Conclusion

A common challenge in ocean engineering is to accurately model waves in an infinite ocean using a limited computational domain. Unlike traditional methods that rely on a wide damping zone, the SCBEM does not alter the free surface conditions surrounding the BEM truncation boundaries. Instead, it modifies the BVP by using a transition function. SCBEM splits the original BVP into two parts: a near-field part solved by the BEM and a far-field part solved by the HOS. The SCBEM combines the benefits of BEM in modeling complex geometries and HOS in computational efficiency. As a result, the simulated area can be enlarged with the extension of the HOS layer while keeping the BEM domain unchanged, leading to improved computational efficiency.

To evaluate the accuracy of the SCBEM, simulations of regular waves with varying wavelengths are carried out. The results of these simulations show that the wave damping method is insufficient to prevent wave reflection at the truncation boundary for waves with wavelengths greater than the width of the damping zone. Conversely, the SCBEM is able to maintain wave transmission through the BEM truncation boundaries with minimal error, even for waves with large wavelengths. The SCBEM is then tested on cases featuring strong nonlinearities, including modulated wave trains and focused waves. Despite the challenging nature of these cases, with modulated wave trains exceeding the length of the BEM domain and focused waves containing numerous wave components, the results obtained from the SCBEM simulations are in good agreement with published literature, thereby confirming the accuracy of the SCBEM in modeling nonlinear wave interactions. Finally, the performance of the SCBEM in simulating hydrodynamic phenomena in the presence of obstacles is validated through the simulation of wave diffraction around a cylinder. The results show consistent agreement with previous nonlinear studies and experiments, indicating that the SCBEM offers a promising approach for simulating the nonlinear hydrodynamics of large-scale structures with reduced computational effort.

The methodology presented in this paper is focused on decomposing the boundary conditions for infinite water depths. However, similar strategies can also be adapted to deal with finite water depths or varying sea bottom topographies. Furthermore, the solvers for the two separated BVPs do not need to be limited to HOS and BEM. Alternative solutions, such as using the Boussinesq model in place of HOS or a spatial-based method such as FVM to solve the near-field region, can also be employed.

Declaration of Competing Interest

The authors declare that they have no known competing financial interests or personal relationships that could have appeared to influence the work reported in this paper.

Acknowledgments

This work was supported by the Fundamental Research Funds for the Central Universities and the YEQISUN Joint Funds of the National Natural Science Foundation of China (Grant no. U2141228).

References

[1] A. Abbasnia, C.G. Soares, Ocean Eng. 152 (2018) 210–222.
[2] F. Coslovich, M. Kjellberg, M. Östberg, C.-E. Janson, Ocean Eng. 229 (2021) 108935, doi:10.1016/j.oceaneng.2021.108935.
[3] Y. Tang, S.-L. Sun, H.-L. Ren, Ocean Eng. 223 (2021) 108705, doi:10.1016/j.oceaneng.2021.108705.
[4] A. Abbasnia, M. Karimirad, D. Friel, T. Whittaker, Ocean Eng. 257 (2022) 111320.
[5] M. Irannezhad, A. Eslamdoost, M. Kjellberg, R.E. Bensow, Ocean Eng. 246 (2022) 110410.
[6] Y.-L. Shao, O.M. Faltinsen, J. Comput. Phys. 274 (2014) 312–332.
[7] V. Rokhlin, J. Comput. Phys. 60 (2) (1985) 187–207.
[8] J. Barnes, P. Hut, Nature 324 (6096) (1986) 446–449.
[9] D. Givoli, J. Comput. Phys. 94 (1) (1991) 1–29.
[10] J. Romate, J. Comput. Phys. 99 (1) (1992) 135–145, doi:10.1016/0021-9991(92)90281-3.
[11] S.V. Tsynkov, Appl. Numer. Math. 27 (4) (1998) 465–532.
[12] D. Givoli, Wave Motion 39 (4) (2004) 319–326.
[13] M. Israeli, S.A. Orszag, J. Comput. Phys. 41 (1) (1981) 115–135.
[14] I. Orlanski, J. Comput. Phys. 21 (3) (1976) 251–269.
[15] J. Broeze, J. Romate, J. Comput. Phys. 99 (1) (1992) 146–158.
[16] Z.-P. Liao, Wave Motion 24 (2) (1996) 117–138, doi:10.1016/0165-2125(96)00010-8.
[17] K. Dgaygui, P. Joly, SIAM J. Appl. Math. 54 (1) (1994) 93–131.
[18] G.I. Jennings, S. Karni, J.B. Rauch, J. Comput. Phys. 276 (2014) 729–739, doi:10.1016/j.jcp.2014.02.032.
[19] A. Mueller, J. Comput. Phys. 359 (2018) 283–295.
[20] A. Clément, J. Comput. Phys. 126 (1) (1996) 139–151, doi:10.1006/jcph.1996.0126.
[21] G. Xu, W. Duan, Appl. Ocean Res. 42 (2013) 136–143.
[22] W.M. Lin, D. Yue, 18th Symp. on Naval Hydrody. Ann Arbor, 1990, 1990.
[23] S. Zhang, W.M. Lin, K. Weems, et al., A hybrid boundary-element method for non-wall-sided bodies with or without forward speed, in: 13th International Workshop on Water Waves and Floating Bodies, The Netherlands, 1998, pp. 179–182.
[24] X. Chen, R. Zhu, C. Ma, J. Fan, Ocean Eng. 114 (2016) 142–153.
[25] P. Wang, Y. Yao, M.P. Tulin, Int. J. Numer. Methods Fluids 20 (12) (1995) 1315–1336, doi:10.1002/fld.1650201203.
[26] P.C. De Haas, P.J. Zandbergen, J. Comput. Phys. 129 (2) (1996) 332–344, doi:10.1006/jcph.1996.0253.
[27] W. Bai, R. Eatock Taylor, Appl. Ocean Res. 29 (1–2) (2007) 55–71, doi:10.1016/j.apor.2007.05.005.
[28] W. Bai, R. Eatock Taylor, Ocean Eng. 36 (3–4) (2009) 223–236, doi:10.1016/j.oceaneng.2008.11.003.
[29] T. Geng, H. Liu, F. Dias, Phys. Fluids 33 (3) (2021) 037129.

[30] V.E. Zakharov, J. Appl. Mech. Tech. Phys. 9 (2) (1968) 190–194, doi:10.1007/BF00913182.
[31] X. Zhang, P. Bandyk, R.F. Beck, Appl. Ocean Res. 32 (4) (2010) 471–482, doi:10.1016/j.apor.2010.10.003.
[32] J.L. Hess, A.O. Smith, Prog. Aerosp. Sci. 8 (1967) 1–138.
[33] D.G. Dommermuth, D.K.P. Yue, J. Fluid Mech. 184 (1987) 267–288, doi:10.1017/S002211208700288X.
[34] B.J. West, K.A. Brueckner, R.S. Janda, D.M. Milder, R.L. Milton, J. Geophys. Res. 92 (C11) (1987) 11803, doi:10.1029/JC092iC11p11803.
[35] A. Finkelstein, Commun. Pure Appl. Math. 10 (4) (1957) 511–522.
[36] G. Wu, Direct Simulation and Deterministic Prediction of Large-scale Nonlinear Ocean Wave-field, Massachusetts Institute of Technology. Department of Ocean Engineering, 2004 Ph.D. thesis.
[37] D.C. Kring, Time Domain Ship Motions by a Three-Dimensional Rankine Panel Method, Massachusetts Institute of Technology, 1994 Ph.D. thesis.
[38] S. Boo, Ocean Eng. 29 (5) (2002) 475–493.
[39] J.D. Fenton, J. Waterway, Port, Coast., Ocean Eng. 111 (2) (1985) 216–234.
[40] T.B. Benjamin, J.E. Feir, J. Fluid Mech. 27 (3) (1967) 417–430.
[41] A. Toffoli, O. Gramstad, K. Trulsen, J. Monbaliu, E. Bitner-Gregersen, M. Onorato, J. Fluid Mech. 664 (2010) 313–336, doi:10.1017/S002211201000385X.
[42] A. Iafrati, A. Babanin, M. Onorato, J. Comput. Phys. 271 (2014) 151–171, doi:10.1016/j.jcp.2013.12.045.
[43] T.B. Johannessen, C. Swan, On the nonlinear dynamics of wave groups produced by the focusing of surface–water waves, in: Proceedings of the Royal Society of London. Series A: Mathematical, Physical and Engineering Sciences, vol. 459, The Royal Society, 2003, pp. 1021–1052.
[44] Ocean Engineering Committee, Technical Report, Copenhagen, Denmark, 2014.
[45] L. Sun, J. Zang, L. Chen, R.E. Taylor, P. Taylor, Appl. Ocean Res. 59 (2016) 650–662.